Chemical Science

EDGE ARTICLE

View Article Online
View Journal

Check for updates

Cite this: DOI: 10.1039/d5sc07530k

All publication charges for this article have been paid for by the Royal Society of Chemistry

Received 28th September 2025
Accepted 16th December 2025

DOI: 10.1039/d5sc07530k

rsc.li/chemical-science

Membrane-free two-step water electrolysis enabled by a stable organic redox mediator

Xiao Liu,[a] Jinlan Tang,[a] Duan Bin, *[a] Qiang Huang, [a] Congcong Li,[a] Linyan Su,[a] Wei Qin,[a] Yu Ge,[a] Xingru Chen,[a] Hongbin Lu,[a] BeiBei Yang*[a] and Yonggang Wang *[b]

Electrochemical decoupled water splitting utilizes a solid-state redox mediator (SSRM) to reversibly store proton–electron pairs, thereby separating hydrogen and oxygen evolution without the use of a membrane and promoting the conversion of sustainable energy sources into hydrogen. However, the widespread application of this approach is currently limited by issues such as the instability and discontinuity of SSRM. Herein, a novel and membrane-free system is designed for decoupled hydrogen production in an acidic medium, based on the use of a highly reversible SSRM on a sustainable quinone-based organic polymer (P-ACD). Due to intramolecular hydrogen bonds, the P-ACD electrode with a low P-ACD loading (1–2 mg cm^{-2}) exhibits a high discharge specific capability (215.32 mAh g^{-1} at 0.2 A g^{-1}), ultrafast chargeability (86.90 mAh g^{-1} at 100 A g^{-1}, just 3.12 s), and exceptional cyclability over 30 000 cycles. More importantly, two-step water electrolysis under high P-ACD loading achieves a remarkable coulombic efficiency of nearly 100% even after 600 consecutive cycles, whilst concurrently exhibiting favorable cycle stability for hydrogen production that surpasses 184 h. Consequently, this system provides a new avenue for achieving operational flexibility and membrane-free hydrogen production.

Introduction

Green hydrogen can greatly contribute to carbon neutrality as it possesses many prominent benefits, such as a high energy density and zero pollution emissions.[1–4] Water electrolysis is capable of producing eco-friendly hydrogen with an impressive energy density of 143 MJ kg^{-1}, and it is estimated that by 2050, approximately 70% of hydrogen will be produced *via* this process, powered by renewable energy sources.[5–7] Among the various water electrolysis technologies, proton exchange membrane (PEM) electrolyzers hold notable advantages, including high hydrogen purity and current density, superior efficiency and a compact cell design.[8,9] However, this type of electrolysis faces challenges such as high costs arising from the PEM, and poor durability stemming from the sluggish anodic oxygen evolution reaction (OER) and the degradation of catalysts in acidic media,[10] thus widely limiting its practical applications. Noticeably, a persistent challenge in conventional water-splitting systems is gas crossover at low current densities, which can lead to the formation of an explosive H_2/O_2 mixture.[11] Thus, it is imperative to develop membrane-free acidic water electrolysis, wherein the release of H_2 and O_2 occurs independently in both time and space. With these considerations in mind, Cronin *et al.*[11] pioneered the utilization of polyoxometalate $H_3PMo_{12}O_{40}$ as a solid-state redox mediator (SSRM) and afforded some new insight into achieving the temporal and spatial decoupling of the H_2 and O_2 evolution in PEM water electrolysis. In addition, some inorganic redox mediators, *e.g.*, $Ni(OH)_2$ (nickel hydroxide),[12] $H_4[SiW_{12}O_{40}]$ (silicotungstic acid),[13] and $Na_4[Fe(CN)_6]$ (sodium ferrocyanide)[14] have been explored for decoupled water electrolysis. It is worth noting that organic materials, endowed with high design flexibility, environmental sustainability, and cost efficiency, have rarely gained widespread utilization as SSRM materials in decoupled water electrolysis.[15–17]

Encouragingly, quinone-based organic compounds are known for their high theoretical capacities, advantageous redox potentials, and swift reaction kinetics, which can be attributed to the enolization reaction that occurs as part of the carbonyl redox chemistry of the C=O and C–O$^-$ groups.[18] Ma *et al.*[19] have presented pyrene-4,5,9,10-tetraone (PTO) as an SSRM material to separate the HER and OER in an acidic environment, achieving an electrolysis time of approximately 70.7 h for cycle stability. Meanwhile, Huang *et al.*[20] have designed a pseudocapacitive electrode based on dibenzo[*b*,*i*]phenazine-5,7,12,14-tetrone (DPT) that is capable of decoupled acidic water electrolysis, with the electrolysis time required for cycle stability reaching over 100 h. Although the use of the above organic

---

[a] School of Chemistry and Chemical Engineering, Nantong University, Nantong, 226019, China. E-mail: dbin17@fudan.edu.cn; yangbeibei@ntu.edu.cn

[b] Department of Chemistry, Shanghai Key Laboratory of Molecular Catalysis and Innovative Materials, Institute of New Energy, iChEM (Collaborative Innovation Center of Chemistry for Energy Materials), Fudan University, Shanghai 200433, China. E-mail: ygwang@fudan.edu.cn

electrodes in SSRM systems to decouple water electrolysis has been reported, they still suffer from solubility issues and have demonstrated limited cycling lifetimes (<10 000 cycles) and decoupling times (<150 h). Undoubtedly, the long-term stability of SSRMs is vital for continuous water electrolysis, which motivates the development of sustainable organic electrodes with low aqueous solubility. Structurally, organic carbonyl compounds tend to dissolve in electrolytes mainly because of their inherent structural characteristics, like electron-rich aromatic units, which closely align with the polarity of the electrolytes, fostering strong interactions and subsequent dissolution of the material, thereby impairing cycling stability.[21,22] Currently, the formation of stable intramolecular hydrogen bonds (HBs) utilizing carbonyl groups represents a straightforward and effective strategy, achieved through molecular engineering design, for tackling problems such as unsatisfactory stability in carbonyl-containing organic compounds.[23] In this regard, it is highly desirable to develop efficient carbonyl compounds for use in the continuous membrane-free acid water electrolysis.

Herein, an intramolecular hydrogen bonding (HB) strategy is reported, where the carbonyl groups and secondary amine groups act as multi-active centers, triggering the formation of intramolecular HBs. The intramolecular HBs in a quinone-based organic polymer (P-ACD) used at a low loading in an electrode not only inhibit dissolution to enhance stability (over 30 000 cycles at 4 A g^{-1}) but also strengthen the π-conjugation effect to accelerate charge transfer, thereby improving rate capability (86.90 mAh g^{-1} at 100 A g^{-1}). In addition, the electrode with a low P-ACD loading delivers a high discharge specific capacity of 215.32 mAh g^{-1}. Theoretical calculations suggest that the P-ACD experiences a sequential one-electron redox process during the reversible H^+ storage process. Then, P-ACD functions as a SSRM, effectively separating the HER and OER during acidic water electrolysis. In this design, H_2 generation involves the cathodic reduction of H^+ and the anodic oxidation of P-ACD-2H (P-ACD-2H → P-ACD), whereas O_2 production depends on the cathodic reduction of P-ACD (P-ACD → P-ACD-2H) and the anodic oxidation of H_2O. Interestingly, this decoupled acidic water electrolysis system can be combined with a commercial photovoltaic power generation system, facilitating the direct conversion of solar energy and water into hydrogen.

Result and discussion

The P-ACD was synthesized using a straightforward process with a molar ratio of 5 : 1 between the two organic monomers, 1,4-benzoquinone (monomer BQ) and 1,5-diaminonaphthalene (monomer 1,5-NAD), leading to the formation of the extended π-conjugated polymeric skeleton with a carbonyl oxygen-containing unit located in the main active area (Fig. S1). This molar ratio, far from merely offsetting reaction losses, proactively optimizes the efficiency of the synthesis. Using ethanol as the solvent proves advantageous as it can weaken the intensity of the electrostatic attractions and diminish the competition of solvent molecules for the N–H and C=O groups, thereby maintaining the specific intramolecular hydrogen bonding interactions. In the Fourier-transform infrared (FTIR) spectra, the peaks at 3232 and 1573 cm^{-1} correspond to the stretching vibrations of the N–H···O bonds and C=C bonds, respectively (Fig. 1a). The C=O and N–H peaks in P-ACD exhibit an obvious red shift from 1648 to 1629 cm^{-1} and from 3413 to 3361 cm^{-1}, respectively, with respect to the peaks observed in BQ and 1,5-NAD. This behavior is due to the formation of intramolecular HB (C=O···H–N).[24] In parallel, the emergence of a strong peak in the Raman spectra corresponding to the C=O group served as additional evidence for the formation of the quinone structure. As observed in Fig. 1b, the X-ray diffraction (XRD) analysis indicates that P-ACD displayed broader characteristic peaks than the raw materials BQ and 1,5-NAD after the polymerization reaction. Moreover, thermogravimetric (TG) analysis, as depicted in Fig. 1c, revealed that the weight loss of the P-ACD was negligible upon heating to 140 °C, indicating it possesses excellent thermal stability below this temperature. The scanning electron microscopy (SEM) images (Fig. 1d and S2) show that the P-ACD surface morphology was composed of irregularly shaped nanoparticles. In the reduced density gradient (RDG) analysis, significant green spikes (marked by blue dashed circles) in the $(\lambda_2)_\rho$ range of −0.01 to 0.02 a.u. and prominent cyan-blue spikes (highlighted by red dashed circles) in the $(\lambda_2)_\rho$ range of −0.03 to 0.02 a.u. were observed, suggesting intermolecular π–π stacking interactions between adjacent aromatic planes and intramolecular hydrogen bonding within the polymeric framework, respectively (Fig. 1e). As shown in Fig. S3, the localized orbital locator-π (LOL-π) map of the naphthalene ring in P-ACD confirms the extensive conjugation and electron delocalization. Furthermore, as seen in Fig. 1f, the electrostatic surface potential (ESP) mapped on the van der Waals surface of the P-ACD molecule reveals red regions and blue regions, corresponding to nucleophilic attack sites and electrophilic reaction centers, respectively. Specifically, the C=O group was the focus of the negative ESP, indicating a strong electrophilic tendency within this group. Further, a smaller gap (2.04 eV) between the energy levels of the lowest unoccupied molecular orbital (LUMO) and the highest occupied molecular orbital (HOMO), in comparison to BQ (3.93 eV) and 1,5-NAD (4.15 eV), serves as a clear indication of the enhanced overall molecular conjugation and increased electron delocalization. Moreover, this also indicates the capacity of P-ACD for rapid charge transfer, as evidenced by its high electronic conductivity and superior redox kinetics (Fig. 1g).

The proton-storage electrochemical performance of the designed P-ACD (SSRM) was evaluated in detail. The electrochemical activity of the P-ACD electrode was first evaluated in a typical three-electrode system using 1 M H_2SO_4 as the electrolyte. The cyclic voltammograms (CV) of the redox mediator P-ACD were expected to occur between the linear sweep voltammetry (LSV) curves of the HER and OER potentials of the Pt-coated Ti-mesh electrode and RuO_2/IrO_2-coated Ti-mesh electrode, thus confirming that decoupled water electrolysis does occur and that the use of P-ACD is feasible, as depicted in Fig. 2a. It was also noted that the P-ACD typically underwent two successive one-electron reactions (anodic: 0.13, 0.38 V,

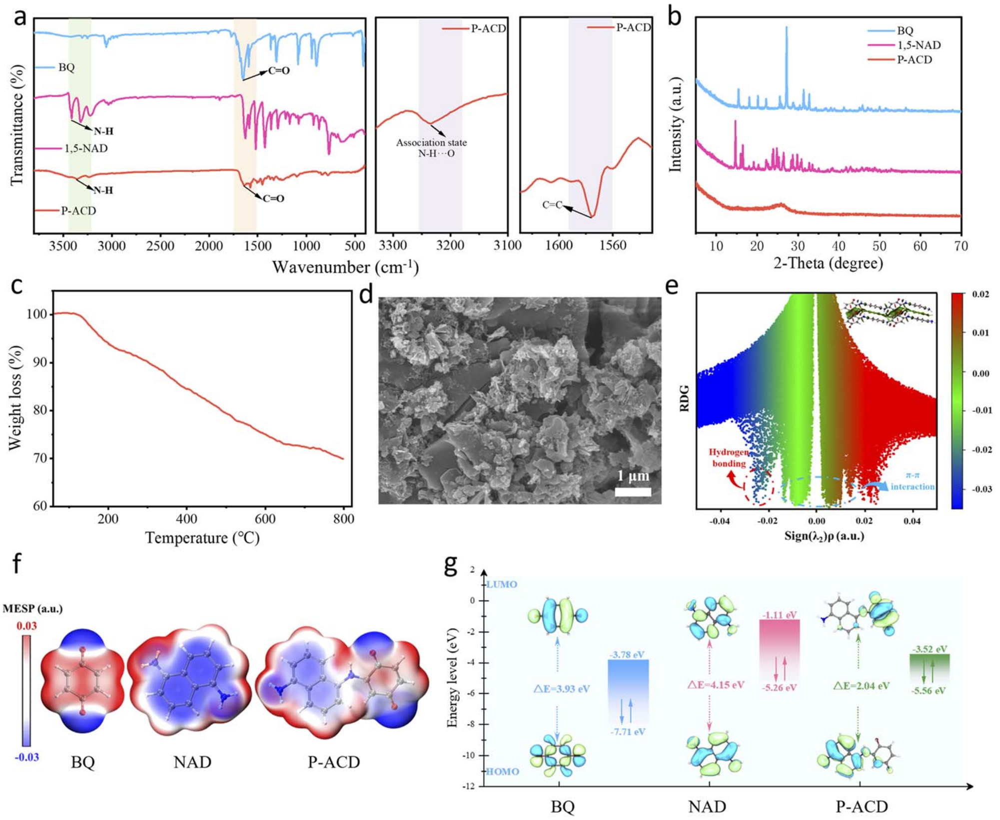

Fig. 1 Synthesis and characterization of P-ACD. (a) FTIR spectra of BQ, 1,5-NAD, and P-ACD molecules. (b) XRD patterns of the BQ, 1,5-NAD, and P-ACD molecules. (c) TGA of the P-ACD polymer under N_2. (d) SEM image of P-ACD. (e) Plots of RDG *versus* sign$(\lambda_2)_\rho$ and the corresponding gradient *iso*-surface of the P-ACD polymer. (f) Calculated ESP distribution of the BQ, 1,5-NAD, and P-ACD molecules. (g) Calculation of the relative HOMO/LUMO energies and optimized structures of the molecules used in the DFT calculations.

cathodic: 0.02, 0.21 V) associated with the reversible formation of P-ACD-AH and P-ACD-2H. Furthermore, CV curves of P-ACD at different scan rates (0.2–5 mV s^{-1}) were performed, as shown in Fig. S4, in which two pairs of redox peaks displayed minimal potential shifts with increasing scan rate. It was found that the relationship between the peak current i and scan rate v could be expressed by the equation $i = av^b$,[25] and the b-values for the two pairs of redox peaks of P-ACD (denoted as a_1/c_1 and a_2/c_2) were calculated as 0.96/0.96 and 0.93/0.93, respectively (Fig. 2b). Strikingly, Fig. 2c and S5 show that the capacitive contribution to the total capacity increased from 76.65% at 0.2 mV s^{-1} to 85.05% at 5 mV s^{-1}, demonstrating the pseudocapacitive-dominated charge storage behavior of the P-ACD electrode, which is underpinned by fast ionic uptake/removal kinetics.[26,27] As can be observed from Fig. S6a and b, the exceptional ionic diffusion capability of the P-ACD electrode was additionally validated through electrochemical impedance spectroscopy (EIS) tests.[28] Furthermore, electrochemical impedance spectroscopy was utilized to analyze the kinetic behavior across distinct voltage stages of the discharge curve (Fig. S6c and d). Notably, the calculated diffusion coefficient in Point 1 (2.22×10^{-9} cm^2 s^{-1}) is significantly higher than that in Point 2 (4.30×10^{-10} cm^2 s^{-1}), suggesting different ions are inserted during the two different discharge processes. Fig. 2d demonstrates the galvanostatic charge/discharge (GCD) curves under different current densities of the P-ACD in an H^+ ion electrolyte. The specific capacities of the P-ACD electrode were measured to be 179.04, 177.94, 169.02, 163.18, 157.99, 153.42, 147.42, 142.51, 137.75, 132.52, 126.30, 118.81, 109.48, 98.63, and 86.90 mAh g^{-1} at current densities of 0.2, 0.5, 1, 2, 5, 10, 20, 30, 40, 50, 60, 70, 80, 90, and 100 A g^{-1}, respectively. Moreover, the rate capability of the P-ACD electrode was further evaluated, and it exhibited favorable rate performance (swift proton and electron absorption/donation capabilities) (Fig. S7). The charge and discharge curves obtained from the GCD analysis demonstrate a high degree of symmetry at all current densities, indicating a highly reversible energy storage process. Notably, an area-specific capacitance of 1370.44 mF cm^{-2} is achieved at a current density of 0.30 mA cm^{-2}, highlighting its superior energy storage capacity (Fig. S8). Fig. S9 presents further calculations of the LUMO and HOMO for the P-ACD polymer, alongside a comparative analysis of the energy levels of other organic polymers. Impressively, the energy gap observed was markedly narrower compared to those of previously reported polymers with comparable molecular frameworks. Typically, a diminished HOMO–LUMO energy gap (2.04 eV) correlates with enhanced conductivity, indicating that P-ACD possesses the capability for rapid charge-carrier migration and superior reaction dynamics, which is in good agreement with the results of the rate capability tests.[29,30] By contrast, the discharge

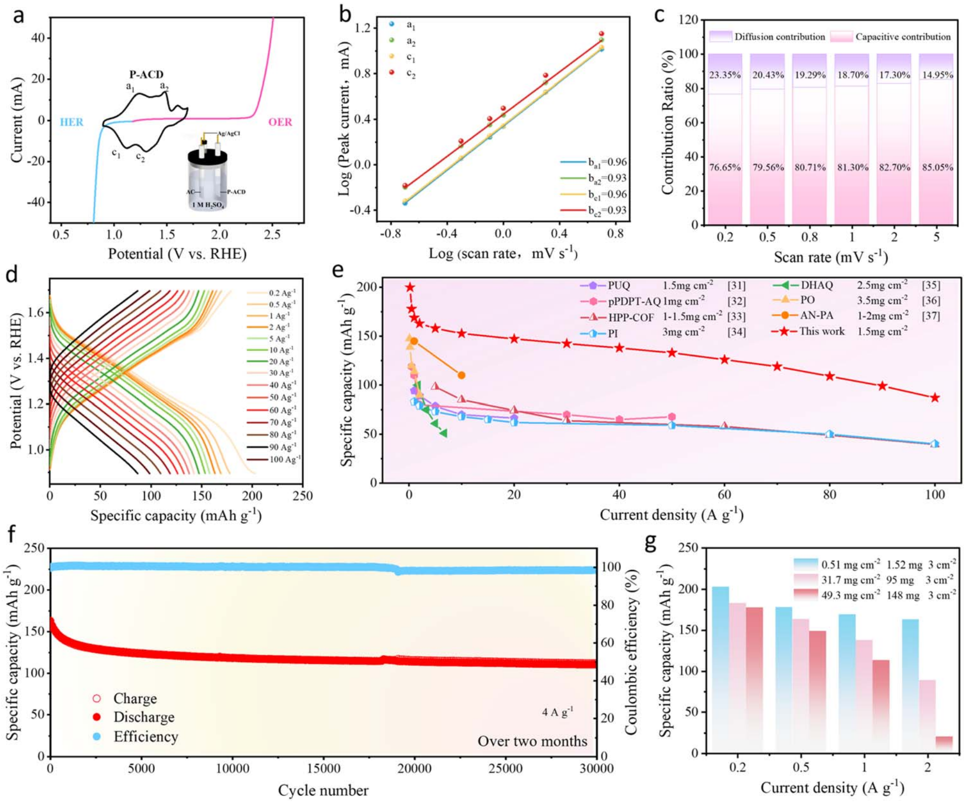

Fig. 2 Electrochemical performance of the P-ACD electrode (mass loadings of 1–2 $mg_{P\text{-}ACD}$ cm^{-2}). (a) CV curve of the P-ACD film electrode (black line), the LSV data of the Pt-coated Ti-mesh electrode for the HER (blue line) and the LSV data of the commercially available RuO_2/IrO_2-coated Ti-mesh electrode for the OER (pink line) at a scan rate of 5 mV s^{-1} in 1 M H_2SO_4. (b) The *b*-values are calculated by linearly fitting the log current *vs.* the log scan rate. (c) Percentages of capacitive contribution at different voltage scan rates. (d) GCD curves of the P-ACD-electrode at different current densities from 0.2 to 100 A g^{-1}. (e) Comparison of rate performance with other reported proton-storage electrodes (mass loadings of 1–3.5 mg cm^{-2}). (f) Long-term cycling stability of the P-ACD electrode at a current density of 4 A g^{-1}. (g) Rate performance of the P-ACD electrode with different mass loadings (0.51–49.3 $mg_{P\text{-}ACD}$ cm^{-2}).

capacity of P-ACD, measured at various current densities, greatly exceeded that of most proton-storage electrodes found in other reported materials, as depicted in Fig. 2e.[31–37] As shown in Fig. S10, the P-ACD electrode exhibits a capacity retention of approximately 80% at 0.5 A g^{-1} over 400 cycles. Note that, the P-ACD electrode also achieved unprecedented cycling stability of up to 30 000 cycles at 4 A g^{-1}, with a capacity decay rate of only 0.0023% per cycle, as evidenced in Fig. 2f. The results shown in Fig. S11 and S12 systematically demonstrate the cycling stability of the P-ACD electrode using Nyquist plots and CV profiles over multiple cycles (1st, 5th, 10th, 15th, and 20th). The electrochemical performance remains essentially unchanged, retaining its initial level even after 20 cycles. Notably, it was clearly observed that when the P-ACD electrode was immersed in 1 M H_2SO_4 and 2 M H_2SO_4 electrolytes, it did not dissolve, thereby attesting to its exceptional chemical stability (Fig. S13). As shown in Fig. S14, even after long-term cycling, the P-ACD polymer was impressively stable in a 1 M H_2SO_4 electrolyte without decomposition or dissolution, confirming its excellent structural stability for the repeated storage of protons. The rate performance of the P-ACD electrodes with different mass loadings is shown in Fig. 2g and S15. When the mass loading was increased to 31.70 mg cm^{-2} and 49.30 mg cm^{-2}, the corresponding electrodes still delivered promising capacities of 183.06 mAh g^{-1} and 177.69 mAh g^{-1}, respectively. These results indicate that the P-ACD electrodes can maintain their high-rate performance even under very high mass loadings. Additionally, as shown in Fig. S16, the highly symmetric charge–discharge curves within the current density range of 6.33 to 98.67 mA cm^{-2} demonstrate excellent charge–discharge reversibility. Additionally, the P-ACD electrode with a high mass of 49.3 mg cm^{-2}, shows a favorable lifetime and retains an 88.8% capacity after 200 cycles at a current density of 0.67 A g^{-1} (as shown in Fig. S17). Taken together, the process of decoupled water electrolysis is integrated with a prospective SSRM candidate that is characterized by exceptional redox cyclability and high stability in acidic solution.

As noted earlier, P-ACD presents excellent reversible electron and proton donor/acceptor activity with a redox-active center thermodynamically positioned between the onset potentials of the OER and HER. The P-ACD electrode can also mitigate pH fluctuations in the electrolyte during HER/OER processes, thereby acting as an ideal SSRM for acidic water electrolysis. To prove the viability of the decoupled hydrogen production, a hybrid energy device was assembled from a commercially available Pt-coated Ti-mesh electrode used for the HER and a commercially available RuO_2/IrO_2-coated Ti-mesh electrode used for the OER, with the incorporation of a P-ACD film electrode as the redox mediator, as is shown in Fig. S18. A general illustration of the SSRM approach based on the reversible enolization of the solid-state P-ACD is given in Fig. 3a. The P-ACD initially underwent a reversible reduction process to attain an anionic intermediate through electron acquisition, followed by proton coordination in the 1 M H_2SO_4, ultimately forming P-ACD-2H *via* a coordination reaction. In Step 1, electrochemical reoxidation of the reduced SSRM (P-ACD-2H) then released the protons and electrons (P-ACD) to give H_2 at the Pt-coated Ti-mesh electrode. In Step 2, the protons and electrons were used to reversibly reduce and protonate the SSRM (P-ACD-2H) to give O_2 at the RuO_2/IrO_2-coated Ti-mesh electrode.

To verify the practicability of decoupled amphoteric water electrolysis, chronopotentiometry measurements were conducted in 1 M H_2SO_4 to investigate the performance of this decoupled system, with applied current densities ranging from 1.67 to 100 mA cm^{-2} (Fig. 3b–e and S19a–c). The performance under varying electrolysis currents demonstrates the operational flexibility of the system, in which the electrolysis duration progressively decreases with increasing current (with the mass of P-ACD held constant, the electrolysis time for each step varies with the applied current). Furthermore, the voltages of both Step 1 and Step 2 were derived from the potential difference between the anode and cathode. The chronopotentiometry curves, showing anodic and cathodic potentials *versus* time, were studied during the electrolysis process at a current density of 1.67 mA cm^{-2} with a step time of 10 800 s, and the results are shown in Fig. 3b. Specifically, in Step 1 (H_2 generation), the average operating voltage (0.472 V) was calculated as the difference between the P-ACD oxidation anode potential (1.340 V *vs.* RHE) and the H^+ reduction cathode potential (0.868 V *vs.* RHE). For Step 2 (O_2 generation), the voltage increased to 1.092 V, as determined by the H_2O oxidation anode potential (2.467 V *vs.* RHE) minus the HATN reduction cathode potential (1.375 V *vs.* RHE). Furthermore, the acidic water electrolysis cell was investigated with an applied current of 100 mA cm^{-2} and a fixed step time of 80 s. The cell voltages during

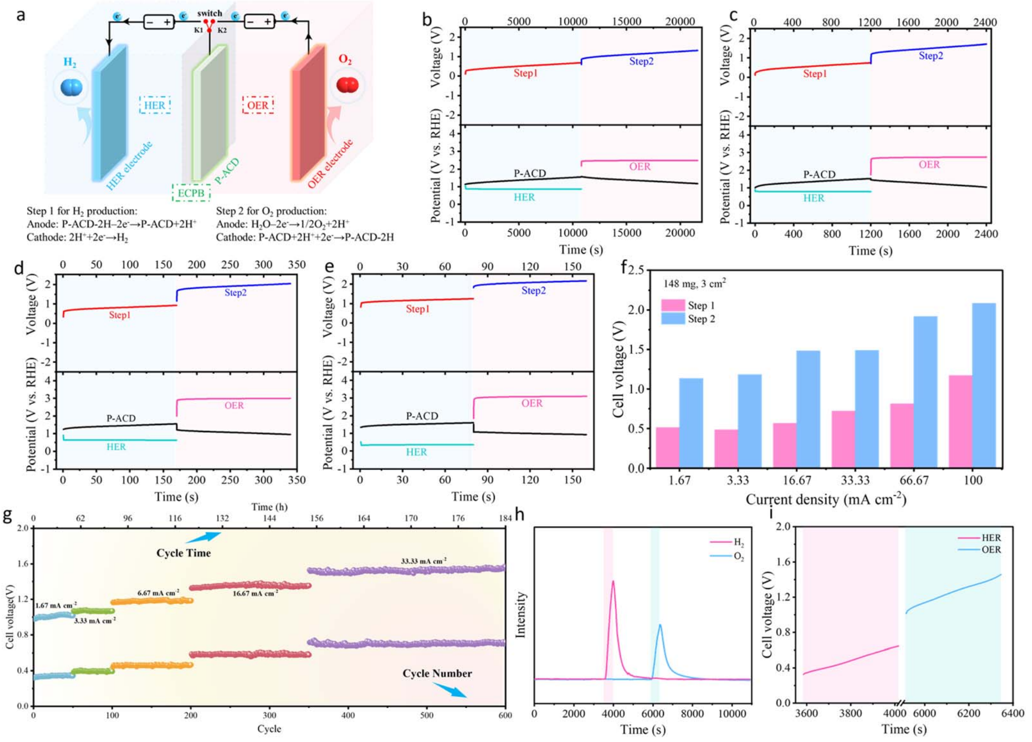

Fig. 3 The decoupled water electrolysis system using the P-ACD electrode as a redox mediator under high P-ACD loading. (a) Schematic of the decoupled water electrolysis system using the P-ACD electrode as the redox mediator. Chronopotentiometry curves of the decoupled cell at current densities of (b) 1.67 mA cm^{-2}, (c) 16.67 mA cm^{-2}, (d) 66.67 mA cm^{-2} and (e) 100 mA cm^{-2} with step times of 10 800 s, 1200 s, 170 s and 80 s, respectively. The voltages for H_2 production (Step 1) and O_2 production (Step 2) are labelled by the red and blue lines, respectively. Chronopotentiometry data (potential *versus* time) of the OER electrode (pink line), HER electrode (green line) and P-ACD electrode (black line) are provided (mass loadings of 49.3 mg$_{\text{P-ACD}}$ cm^{-2}). (f) Cell voltages of the decoupled water electrolysis cells at each step under different applied currents utilizing the P-ACD electrode with a mass loading of 49.3 mg$_{\text{P-ACD}}$ cm^{-2} as the redox mediator (the cell voltage of each cycle is derived from the average value of its chronopotentiometry data). (g) The stability performance of separate H_2/O_2 generation at 1.67 mA cm^{-2}, 3.33 mA cm^{-2}, 6.67 mA cm^{-2}, 16.67 mA cm^{-2}, and 33.33 mA cm^{-2} is evaluated, with the cell voltage for each cycle calculated as the average value obtained from the chronopotentiometry data (mass loadings of 32.7 mg$_{\text{P-ACD}}$ cm^{-2}). (h) The production of high-purity H_2 (Step 1, indicated by the pink line) and O_2 (Step 2, indicated by the blue line) is demonstrated by *in situ* DEMS analysis and (i) the corresponding chronopotentiometry curves (voltage *versus* time) of the electrolytic cell at an applied current density of 33.33 mA cm^{-2}.

Step 1 (H_2 production) and Step 2 (O_2 production) were measured to be 1.13 V and 2.04 V, respectively, which correspond to the potential differences between the anode and cathode, as seen in Fig. 3e. Notably, the P-ACD electrode can operate normally under a high current density of 100 mA cm^{-2}, which is attributed to its pseudocapacitive control. This control endows the electrode with rapid kinetics and high capacity, directly enhancing the overall rate of the decoupled electrolysis, especially under high current density conditions.[20] As analyzed above, the fact that the electrolysis times for Step 1 and Step 2 remained identical irrespective of the current employed suggests that the electrolytic system achieved a coulombic efficiency of 100%. Remarkably, at an electrolysis current density of 1.67 mA cm^{-2}, the cell voltages for Step 1 and Step 2 of the electrolytic cell are 0.51 and 1.13 V, respectively, achieving an energy efficiency of 75%, as depicted in Fig. 3f. The photographs of Step 1 and Step 2 are presented in Fig. S20 and the corresponding videos illustrating the independent generation of H_2 and O_2 are provided in Videos S1 and S2. One can notice that the P-ACD, as an established electrode material, exhibits its high energy efficiency along with a long-lasting cycle life (184 h). The stability of the electrochemical cell was evaluated to be over 600 cycles at applied currents of 1.67 mA cm^{-2}, 3.33 mA cm^{-2}, 6.67 mA cm^{-2}, 16.67 mA cm^{-2}, and 33.33 mA cm^{-2}, as shown in Fig. 3g. Impressively, electrolysis was carried out with varying currents and step times, *i.e.*, 1.67 mA cm^{-2} with a step time of 4000 s for 50 cycles, 3.33 mA cm^{-2} with a step time of 2400 s for 50 cycles, 6.67 mA cm^{-2} with a step time of 1200 s for 100 cycles, 16.67 mA cm^{-2} with a step time of 800 s for 150 cycles, and 33.33 mA cm^{-2} with a step time of 400 s for 250 cycles. It was observed that the cell voltages in both Step 1 and Step 2 remained almost unchanged, indicating the exceptional stability of the system for H_2 and O_2 production. This is because the P-ACD electrode contains intramolecular HBs, which enhance intramolecular interaction forces and reduce its solubility.

To ascertain the purity of the hydrogen and oxygen generated during the individual steps, *in situ* differential electrochemical mass spectrometry (DEMS) was utilized for the real-time analysis of gas evolution during the comprehensive water electrolysis process, at a consistent applied current density of 33.33 mA cm^{-2} (see the Experimental Section for details). There was a rapid increase in the baseline signal intensity of H_2, whereas the O_2 baseline signal held steady, which concussively indicated that only the HER took place in Step 1, with no observed OER occurring. Afterwards, the system was allowed to rest and was flushed with pure N_2 to eliminate any residual O_2. Likewise, as Step 2 electrolysis commenced, the O_2 baseline displayed a sharp upward trend, while the H_2 baseline signal stayed unchanged, serving as confirmation that Step 2, dedicated to OER, proceeded without the simultaneous occurrence of any HER. Taken together, these data implied that O_2 and H_2 evolution can be successfully decoupled from each other using P-ACD, thereby permitting direct atmospheric discharge of generated O_2 while inherently avoiding H_2 co-production (see the DEME data diagram in Fig. 3h and the corresponding chronopotentiometry data in Fig. 3i).

The P-ACD/P-ACD-2H electrode—initially unveiled as an SSRM to decouple the O_2 and H_2 evolution processes in acidic water electrolysis—has received significant attention due to its obvious advantages. In light of these results and taking into account the fact that the sequential generation of H_2 and O_2 is beneficial for the flexible utilization of renewable energy, it is reasonable to conclude that integrating a photovoltaic panel with the P-ACD-based decoupling device to form a photovoltaic water electrolysis system would be a worthy endeavor (Fig. 4a, Videos S3 and S4). More interestingly, it can be speculated that by taking advantage of the feature of this system where H_2 and O_2 are produced at different times/locations, solar energy can be utilized for H_2 production during the day, while wind energy can be employed to drive O_2 production at night. To validate this concept, a 12 h cyclic decoupled process was designed: H_2 production during the daytime and O_2 production at night (Fig. 4b and c). Moreover, given that photovoltaic and wind power are characterized by power fluctuations, they are fundamentally incapable of maintaining a constant low current. Therefore, during the hydrogen production process, a varying input current density was applied to simulate the intermittency of renewable energy sources (*e.g.*, solar, wind, *etc.*). Starting from 0.33 mA cm^{-2} and stepping through 0.67, 1.67, 3.33, 8.33, 16.67, 33.33, 66.67, up to 100 mA cm^{-2}, the corresponding cell voltage remained within the range of 0–0.6 V. This result preliminarily demonstrates both the operational flexibility of decoupled water electrolysis over a reasonable timeframe and the continuous operational stability of the system (Fig. S21). Furthermore, to explore the energy consumption of the decoupled water electrolysis system using a proton buffer electrode for H_2, a drainage technique was implemented to measure the volume of H_2 produced over a defined electrolysis period, thus giving us the Faraday efficiency for H_2 production (approximately 99.4%) (Fig. 4d and S22). As illustrated in Fig. 4e, based on the above experimental results, it can be concluded that, compared with traditional one-step water electrolysis, the energy consumption of two-step water electrolysis was slightly lower under specific conditions. It should be noted that this result is derived solely from calculations based on the electrolysis voltage for water splitting and does not account for the additional energy consumption introduced by the third electrode. Fig. S23 demonstrates that the total voltage of the two-step electrolysis under high current is slightly lower than that of the traditional proton exchange membrane electrolysis system, indicating lower energy consumption. Moreover, non-precious electrodes for OER and HER can also be utilized in the decoupled process based on the SSRM (P-ACD) mechanism (see Fig. S24 and corresponding discussions). As depicted in the radar diagram (Fig. 4f), considering all factors, including the time to decouple the cell at 5 mA, mass loading, stability, coulombic efficiency, and applied current density, it is reasonable to expect that P-ACD will outperform the majority of other advanced organic materials, such as PANI, PTPAn, and HATN.[38–40]

To gain deeper insight into the mechanism of the P-ACD/P-ACD-2H reaction, a series of characterizations were conducted to monitor the structure during repeated charge/discharge processes (Fig. 5a). First, FTIR spectra were employed to

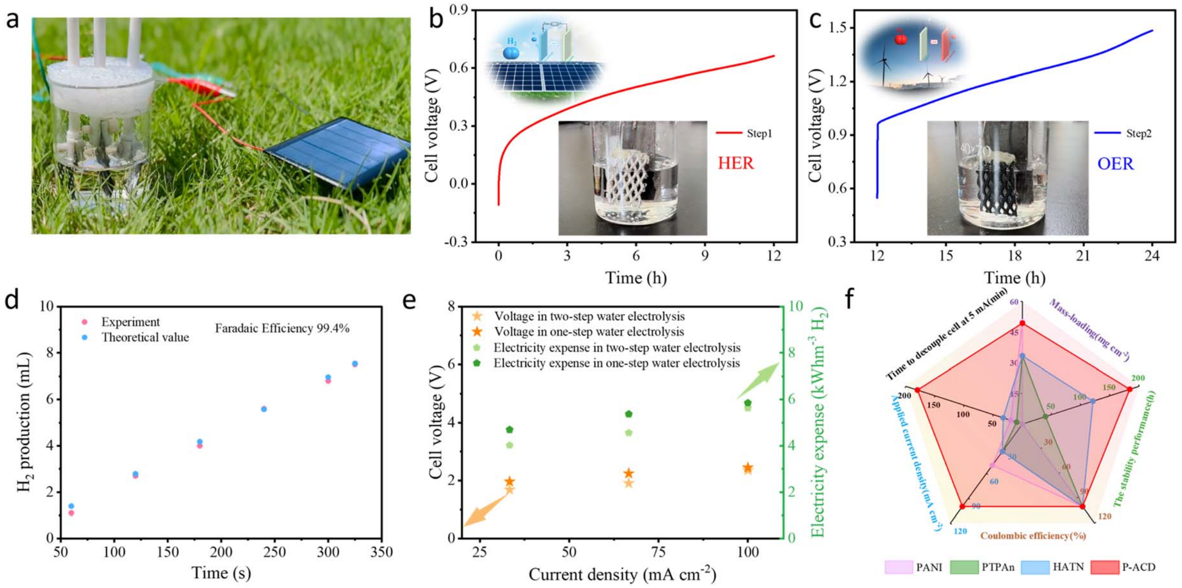

Fig. 4 The decoupled water electrolysis system using the P-ACD electrode as a redox mediator (mass loading of 49.3 $mg_{P\text{-}ACD}$ cm^{-2}). (a) Photo of the OER during photovoltaic water electrolysis under natural sunshine. (b) Hydrogen production (Step 1) during daytime (12 h at 0.33 mA cm^{-2} current density), followed by (c) oxygen production (Step 2) at night (12 h at 0.33 mA cm^{-2} current density). (d) Comparison of the measured and theoretically calculated volume of H_2 during hydrogen production in the HER cell at 66.67 mA cm^{-2}. The hydrogen volume was obtained using the drainage method. (e) The electricity expended for H_2 production at an applied current of 33.3 mA cm^{-2}, 66.7 mA cm^{-2}, and 100 mA cm^{-2}. (f) Comparison of the electrochemical performance of P-ACD and other organic solid-state redox mediators reported in the literature.

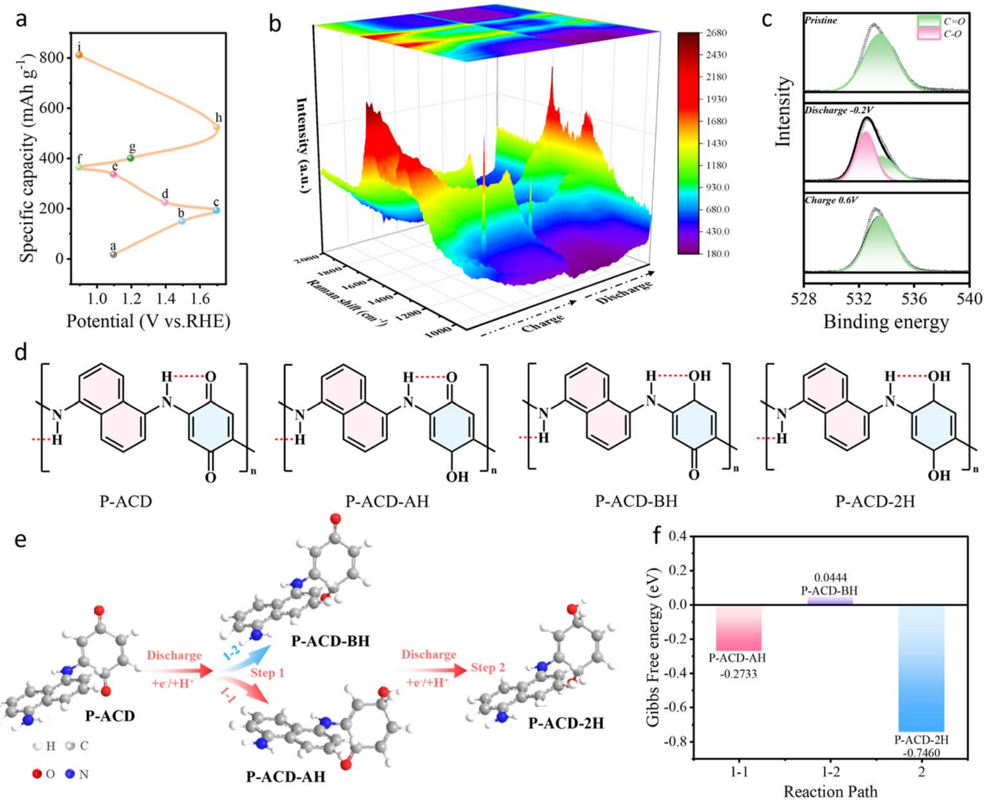

Fig. 5 Structural evolution of the P-ACD electrode during electrochemistry. (a) Initial charge–discharge profiles at 0.5 A g^{-1} of P-ACD. (b) *In situ* Raman spectrum. (c) High-resolution XPS spectra of O 1s at different voltages. (d) The likely configurations of several relevant molecules that are most likely to participate in the P-ACD reduction process. (e) Calculated most probable redox reaction pathways for the reaction between P-ACD and H^+. (f) Structural evolution of H^+-coordinated P-ACD and corresponding ΔG values.

confirm the bonding states during the charge process. Fig. S25 shows that the adsorption peaks at around 1640 cm^{-1} for the C═O groups were weakened continuously during discharging (from point c to f) and enhanced during charging (from point f to h), indicating that the active sites for H^+ coordination were the C═O groups. More intuitively, an *in situ* Raman spectrum also provided additional proof of the activity of the C═O bonds. During charging, the characteristic peak at approximately 1680 cm^{-1} was gradually enhanced but then became progressively weaker during the discharge process, which was attributed to the change in C═O (see Fig. 5b). Aside from the *ex situ* FTIR and *in situ* Raman spectra, *ex situ* X-ray photoelectron spectroscopy (XPS) O 1s (Fig. 5c) was utilized to analyze the P-ACD electrode in pristine, fully discharged and charged states. Notably, the characteristic peak attributed to the C═O group (533 eV) gradually disappeared in the fully discharged state and progressively increased again to a high level in the fully charged state, which was in agreement with the results observed from the *in situ* experiments, thus demonstrating the occurrence of reversible redox reactions between the C═O and C–O groups of the P-ACD electrode during the processes of proton absorption and desorption. Furthermore, DFT calculations were conducted to investigate the redox and electron-conductive mechanisms for P-ACD. The structures of several pertinent molecules that may participate in the reduction process of P-ACD are depicted in Fig. 5d. The simulation results depicting the most probable redox reaction pathways for the reaction between P-ACD and H^+ are shown in Fig. 5e. During the discharging of P-ACD, the protonation of P-ACD occurred in two steps, aligning with the observations from the CV tests. Notably, only part of the P-ACD material underwent further protonation as its C═O group accepts an electron *via* single electron transfer to form an intermediate (C═O$^-$), which then combined with H^+ to yield P-ACD-AH or P-ACD-BH (Step 1). Subsequently, the remaining C═O group in P-ACD was protonated again, resulting in the formation of P-ACD-2H. In the discharge process (Step 1) of the energy-optimized structure of P-ACD (Fig. 5f), the Gibbs free energy change (ΔG) value of reaction 1–1 (−0.2733 eV) was much lower than that of reaction 1–2 (0.0444 eV), suggesting that the one-electron process (P-ACD → P-ACD-AH) was more thermodynamically favorable in Step 1 due to its more negative ΔG value. Afterward, one H^+ charge carrier participated in the redox reaction of Step 2 in the residual carbonyl sites, resulting in the formation of P-ACD-2H. Collectively, the results obtained from the theoretical calculations clearly indicate that P-ACD was subject to a redox process that consists of two consecutive one-electron transfer steps that give it its capacity for H^+ storage.

Conclusions

In summary, the P-ACD/P-ACD-2H redox-coupled hydrogen production system enables membrane-free decoupled acidic water electrolysis, effectively separating hydrogen and oxygen production. Comprehensive *ex situ* and *in situ* characterizations reveal that the P-ACD electrode undergoes decomposition into a hydrogen donor, thereby facilitating a two-proton transfer *via* an enolization reaction. Owing to the presence of intramolecular hydrogen bonding, the system exhibits a high specific capacity, long-term cycling stability, and rapid chargeability. As a result, the decoupled electrolysis cell demonstrates excellent operational stability (exceeding 184 h) and ultrahigh mass loading (up to 49.33 mg cm^{-2}). By integrating this membrane-free decoupled electrolysis design with a commercially available photovoltaic power generation system, spatiotemporally separated hydrogen and oxygen production has been successfully achieved. This work highlights the application of a novel organic polymer as a redox mediator for decoupled hydrogen production and offers valuable insights for the development of high-performance redox systems.

Author contributions

Xiao Liu: conducted the experiments and wrote the initial draft; Jinlan Tang, Qiang Huang, Congcong Li and Linyan Su performed the theoretical calculations; Wei Qin, Yu Ge, and Xingru Chen carried out the formal analysis; Duan Bin, Beibei Yang, and Hongbin Lu were responsible for the conceptualization, reviewing and editing of the article, as well as securing the research funding; Yonggang Wang: assumed the supervisory work, reviewed and edited the article.

Conflicts of interest

There are no conflicts to declare.

Data availability

The data supporting this article have been included as part of the supplementary information (SI). Supplementary information is available. See DOI: https://doi.org/10.1039/d5sc07530k.

Acknowledgements

This work was financially supported by National Natural Science Foundation of China (22309091 and 22225201).

Notes and references

1 J. Tang, C. Su and Z. Shao, *Exploration*, 2024, **4**, 20220112.
2 J. Liang, S. Li, X. Liu, Y. Wan, Y. Xia, H. Shi, S. Zhang, H.-L. Wang, G. Lu, G. Wu, Y. Huang and Q. Li, *Nat. Catal.*, 2024, **7**, 719–732.
3 J. Wei, Y. Shao, J. Xu, F. Yin, Z. Li, H. Qian, Y. Wei, L. Chang, Y. Han, J. Li and L. Gan, *Nat. Commun.*, 2024, **15**, 9012.
4 K. Dong and Q. Yuan, *Chem. Sci.*, 2025, **16**, 9854–9862.
5 J. Li and H. Duan, *Chem*, 2024, **10**, 3008–3039.
6 A. Odenweller, F. Ueckerdt, G. F. Nemet, M. Jensterle and G. Luderer, *Nat. Energy*, 2022, **7**, 854–865.
7 M. N. Lakhan, A. Hanan, Y. Wang, H. K. Lee and H. Arandiyan, *Chem. Sci.*, 2024, **15**, 15540–15564.
8 J. Kibsgaard and I. Chorkendorff, *Nat. Energy*, 2019, **4**, 430–433.
9 E. A. Toledo-Carrillo, M. García-Rodríguez, L. M. Sánchez-Moren and J. Dutta, *Sci. Adv.*, 2024, **10**, eadi3180.

10 Y. Xu, Z. Mao, J. Zhang, J. Ji, Y. Zou, M. Dong, B. Fu, M. Hu, K. Zhang, Z. Chen, S. Chen, H. Yin, P. Liu and H. Zhao, *Angew. Chem., Int. Ed.*, 2024, **63**, e202316029.

11 B. Rausch, M. D. Symes, G. Chisholm and L. Cronin, *Science*, 2014, **345**, 1326–1330.

12 X. Yan, J. Biemolt, K. Zhao, Y. Zhao, X. Cao, Y. Yang, X. Wu, G. Rothenberg and N. Yan, *Nat. Commun.*, 2021, **12**, 4143.

13 J. Lei, J. Yang, T. Liu, R. Yuan, D. Deng, M. Zheng, J. Chen, L. Cronin and Q. Dong, *Chem. - Eur. J.*, 2019, **25**, 11432–11436.

14 W. Li, N. Jiang, B. Hu, X. Liu, F. Song, G. Han, T. J. Jordan, T. B. Hanson, T. L. Liu and Y. Sun, *Chem*, 2018, **4**, 637–649.

15 S. Wu, M. Taylor, H. Guo, S. Wang, C. Han, J. Vongsvivut, Q. Meyer, Q. Sun, J. Ho and C. Zhao, *Angew. Chem., Int. Ed.*, 2024, **63**, e202412455.

16 C. Wang, D. He, H. Wang, J. Guo, Y. Feng, L. Hu, C. Zheng, M. Zhao, X. Wang and Y. Wang, *Adv. Sci.*, 2024, **11**, 2401314.

17 H. Cui, D. Zhang, Z. Wu, J. Zhu, P. Li, C. Li, Y. Hou, R. Zhang, X. Wang, X. Jin, S. Bai and C. Zhi, *Energy Environ. Sci.*, 2024, **17**, 114–122.

18 C. Peng, F. Wang, Q. Chen, X. Yan, C. Wu, J. Zhang, W. Tang, L. Chen, Y. Wang, J. Mao, S. Dou and Z. Guo, *Adv. Funct. Mater.*, 2024, **34**, 2401001.

19 Y. Ma, Z. Guo, X. Dong, Y. Wang and Y. Xia, *Angew. Chem., Int. Ed.*, 2019, **131**, 4670–4674.

20 X. Huang, T. Kong, Z. Li, X. Yu, C. Liu, Z. Wang and Y. Wang, *Adv. Funct. Mater.*, 2025, 2425176.

21 Q. Zhao, Z. Zhu and J. Chen, *Adv. Mater.*, 2017, **29**, 1607007.

22 Z. Song, W. Liu, Q. Huang, Y. Lv, L. Gan and M. Liu, *Chem. Sci.*, 2025, **16**, 16542–16551.

23 C. Ding, Y. Zhao, W. Yin, F. Kang, W. Huang and Q. Zhang, *Angew. Chem., Int. Ed.*, 2025, **64**, e202417988.

24 Z. Lin, H.-Y. Shi, L. Lin, X. Yang, W. Wu and X. Sun, *Nat. Commun.*, 2021, **12**, 4424.

25 Q. Sun, T. Sun, J. Du, K. Li, H. Xie, G. Huang and X. Zhang, *Adv. Mater.*, 2023, **35**, 2301088.

26 S. Xu, J. Wu, X. Wang and Q. Zhang, *Chem. Sci.*, 2023, **14**, 13601–13628.

27 X. Qiu, J. Xu, K. Zhou, X. Huang, M. Liao, Y. Cao, G. Zhou, P. Wei and Y. Wang, *Angew. Chem., Int. Ed.*, 2023, **62**, e202304036.

28 Y. Zhao, K. Feng and Y. Yu, *J. Energy Chem.*, 2025, **102**, 524–533.

29 Z. Song, L. Miao, H. Duan, Y. Lv, L. Gan and M. Liu, *Angew. Chem., Int. Ed.*, 2024, **63**, e202401049.

30 H. Peng, J. Xiao, Z. Wu, L. Zhang, Y. Geng, W. Xin, J. Li, Z. Yan, K. Zhang and Z. Zhu, *CCS Chem.*, 2023, **5**, 1789–1801.

31 M. Zhu, L. Zhao, Q. Ran, Y. Zhang, R. Peng, G. Lu, X. Jia, D. Chao and C. Wang, *Adv. Sci.*, 2022, **9**, 2103896.

32 X. Wang, J. Zhou and W. Tang, *Energy Storage Mater.*, 2021, **36**, 1–9.

33 Y. Lin, H. Cui, C. Liu, R. Li, S. Wang, G. Qu, Z. Wei, Y. Yang, Y. Wang, Z. Tang, H. Li, H. Zhang, C. Zhi and H. Lv, *Angew. Chem., Int. Ed.*, 2023, **62**, e202218745.

34 W. Han, M. Li, Y. Ma and J. Yang, *Electrochim. Acta*, 2022, **403**, 139550.

35 J. Yu, J. Li, Z. Y. Leong, D. Li, J. Lu, Q. Wang and H. Y. Yang, *Mater. Today Energy*, 2021, **22**, 100872.

36 Z. Tie, S. Deng, H. Cao, M. Yao, Z. Niu and J. Chen, *Angew. Chem., Int. Ed.*, 2022, **61**, e202115180.

37 K. C. S. Lakshmi, B. Vedhanarayanan, H.-Y. Cheng, X. Ji, H.-H. Shen and T.-W. Lin, *J. Colloid Interface Sci.*, 2022, **619**, 123–131.

38 J. Wang, L. Ji, X. Teng, Y. Liu, L. Guo and Z. Chen, *J. Mater. Chem. A*, 2019, **7**, 13149–13153.

39 Y. Ma, X. Dong, Y. Wang and Y. Xia, *Angew. Chem., Int. Ed.*, 2018, **57**, 2904–2908.

40 K. Wu, H. Li, S. Liang, Y. Ma and J. Yang, *Angew. Chem., Int. Ed.*, 2023, **135**, e202303563.